FFI RAPPORT

LOW FREQUENCY MODELS FOR LITTORAL SOUND PROPAGATION - A COMPARISON BETWEEN A FINITE ELEMENT MODEL AND A WAVE NUMBER INTEGRATION MODEL

Ommundsen, Atle and Kristiansen, Ulf R.

FFI/RAPPORT-2005/00170

FFI-IV/896/914

Kjeller 18 January 2005

LOW FREQUENCY MODELS FOR LITTORAL SOUND PROPAGATION - A COMPARISON BETWEEN A FINITE ELEMENT MODEL AND A WAVE NUMBER INTEGRATION MODEL

Ommundsen, Atle and Kristiansen, Ulf R.

FFI/RAPPORT-2005/00170

FORSVARETS FORSKNINGSINSTITUTT
Norwegian Defence Research Establishment
P O Box 25, NO-2027 Kjeller, Norway

FORSVARETS FORSKNINGSINSTITUTT(FFI)
Norwegian Defence Research Establishment

P O BOX 25
NO-2027 KJELLER, NORWAY

UNCLASSIFIED

SECURITY CLASSIFICATION OF THIS PAGE
(when data entered)

REPORT DOCUMENTATION PAGE

1) PUBL/REPORT NUMBER	2) SECURITY CLASSIFICATION	3) NUMBER OF PAGES
FFI/RAPPORT-2005/00170	UNCLASSIFIED	25
1a) PROJECT REFERENCE	**2a) DECLASSIFICATION/DOWNGRADING SCHEDULE**	
FFI-IV/896/914	-	

4) TITLE

LOW FREQUENCY MODELS FOR LITTORAL SOUND PROPAGATION - A COMPARISON BETWEEN A FINITE ELEMENT MODEL AND A WAVE NUMBER INTEGRATION MODEL

5) NAMES OF AUTHOR(S) IN FULL (surname first)

Ommundsen, Atle and Kristiansen, Ulf R.

6) DISTRIBUTION STATEMENT

Approved for public release. Distribution unlimited. (Offentlig tilgjengelig)

7) INDEXING TERMS

IN ENGLISH	IN NORWEGIAN
a) Numerical Modeling	a) Numeriske modeller
b) Helmholtz equation	b) Helmholtz ligning
c) Idealized topography	c) Idealiserte topografier
d) Wave number integration	d) Bølgetall integrasjon
e) Finite element	e) Endelige elementer
f) Littoral sound propagation	f) Kystnær lydforplantning

THESAURUS REFERENCE:

8) ABSTRACT

Two different strategies for modeling sound propagation, exploring the Helmholz equation, in underwater acoustics are presented and compared, a finite element and a wave number integration model. The numerical models incorporate both loss from the bottom, due to the sound interaction with the seafloor, and loss at the open ocean boundaries introduced by the need for a finite computational domain. To resolve a general bottom topography the finite element formulation is used. Good comparison between model results for the different models are documented for our idealized test cases.

9) DATE	AUTHORIZED BY	POSITION
18 January 2005	This page only John-Mikal Størdal	Director

ISBN 82-464-0929-8

UNCLASSIFIED

SECURITY CLASSIFICATION OF THIS PAGE
(when data entered)

CONTENTS

page

LOW FREQUENCY MODELS FOR LITTORAL SOUND PROPAGATION - A COMPARISON BETWEEN A FINITE ELEMENT MODEL AND A WAVE NUMBER INTEGRATION MODEL

1 EXECUTIVE SUMMARY

This report concerns sound propagation in fjords and straits. In the **MINOS** project, one of the aims is to develop models for sound propagation in littoral environments. It was early decided to develop two models, one for low frequency propagation and one for high frequency propagation. The two models were respectively named **Duncan** (Ommundsen 2003) and **MacBeth** (Brodtkorb & Jenssen 2002). **Duncan** is based on the so-called finite element model by which detailed modeling of the underwater bathymetry, geometrical structures, and sound speed profiles can be done. The model is however very demanding with respect to computer time and storage, which again limits its usability to low frequencies. It should be understood that neither of these models in their present states can be used for real time calculation of sound transmission in water. They must be considered as exploration tools that will give a physical basis for the K1K2 models used operationally by the navy.

Little experimental and theoretical information exist on sound propagation in fjords and straits over distances up to a few kilometers. Also, most underwater sound propagation computer models are developed for open waters where no side-walls are present, and where the sea bottom is assumed horizontally stratified.

Results from the **Duncan** model have been compared to results from a very different theoretical model for some special cases. The test geometry we have chosen is a simple canal having constant depth and vertical parallel side walls. The side walls are considered not to absorb any sound. The bottom material is sand. Without side walls, such a geometry is termed a Pekeris waveguide. We therefore call our geometry a Pekeris canal. The numerical model which **Duncan** has been tested against is based on the wave number integration technique, a technique which is efficient for simple geometries, but which does not have the flexibility of the finite element model when it comes to modeling complex geometries. The two models give very similar results for our test cases. This gives confidence in the use of **Duncan** for under water calculations.

We have modeled sound propagation up to a distance of 1000m from the source. Our results show that for the Pekeris canal, three frequency regions are of interest. At low frequencies, *i.e.* where the acoustic wavelengths are long compared to the depth and width of the canal, the sound pressure decreases monotonically with distance from the source up to a distance after which the level is almost constant. In an intermediate region, where the wavelengths are of the same order of magnitude as the canal dimensions, strong interference effects will occur. This is seen as clear peaks and troughs at different distances from the source. At high frequencies there is a multitude of interfering waves and the levels appear almost constant in a canal having little damping. Introducing damping artificially in the sea bottom (specifying an acoustic damping in the sand which is unrealistically large), gives us a region close to the source, where the levels on the whole decrease relatively rapidly with distance, and a region further away with sound levels almost

constant.

There is some experimental evidence that sea bottoms in some fjords and straits might be described by a constant normal impedance. A numerical simulation shows that such conditions will make the sound level close to the bottom decrease at a very high rate.

2 INTRODUCTION

The Norwegian Defence Research Establishment is interested in modeling sound propagation in Norwegian coastal water as part of a Norwegian mine-sweeping project. The areas of interest are typically characterized by shallow and confined waters where sound reflections from bottom and sidewalls are likely to influence the field. Most prediction programs for underwater acoustic propagation are developed for deep sea propagation *i.e.* for environments where the sea bottom is assumed to be made up by horizontally stratified layers. In this report however, the focus is on modeling the pressure field in a limited range up to approximately 1 km in confined waters.

The acoustic signature of a ship is typically characterized by peaks caused by the ship's machinery and propeller. Pure tone sources are therefore relevant for the modeling, and the Helmholtz equation is applicable. To resolve the general complex bottom topography, a 3D finite element method was preferred to the more conventional finite difference method. The code was implemented with the aid of Diffpack (Langtangen 1999), an object-oriented C++ framework for solving partial differential equations.

Little systematic information exist on wave propagation in confined waters. In the present study therefore, results from the finite element program have been compared to results using a different technique based on wave number integration. The wave number integration technique is not as flexible as the finite element model in describing 3D geometries. We have therefore chosen as test example a canal having a flat bottom and parallel side walls, named a Pekeris Canal. The geometry can be regarded as a benchmark for this type of propagation. In addition to the assumptions on the geometry, we have assumed the water to be of uniform composition, with constant density and sound speed. Also, the canal walls are assumed infinitely hard with no acoustic absorption. For the distances and frequencies of interest, we have neither assumed sound absorption in the water. These are however effects that might be added in the future versions.

3 THE EQUATIONS

The time scale of the oceanographic changes is much longer than the time scale of the acoustic propagation. It is therefore assumed that the density and speed of sound is independent of time. The linear wave equation for the pressure then reads,

$$\nabla \cdot \left(\frac{1}{\rho} \nabla P \right) - \frac{1}{\rho c^2} \frac{\partial^2 P}{\partial t^2} + \frac{1}{\rho} \beta \frac{\partial P}{\partial t} = 0, \tag{3.1}$$

where P is the pressure, c the sound speed, ρ density and β a damping coefficient. Since the coefficients to the differential operators are independent of time, we can remove the time

dimension from the wave equation by use of the frequency-time Fourier transform pair,

$$\begin{aligned} f(t) &= \frac{1}{2\pi}\int_{-\infty}^{\infty}\hat{f}(\omega)e^{-i\omega t}d\omega, \\ \hat{f}(w) &= \int_{-\infty}^{\infty}f(t)e^{i\omega t}dt, \end{aligned}$$

leading to the frequency domain wave equation (Helmholtz equation) for the frequency of the disturbance, ω:

$$\nabla\cdot\left(\frac{1}{\rho}\nabla\hat{P}\right)+\frac{1}{\rho}(\frac{\omega^2}{c^2}-i\beta\omega)\hat{P}=-S_\omega\delta(x-x_0)\delta(y-y_0)\delta(z-z_0). \tag{3.2}$$

Here S_ω is introduced as the source strength (assuming a point source), $\hat{P}$ the complex acoustic pressure, and i denotes the (so-called imaginary) square root of -1. In our simulations we have no damping, hence $\beta = 0$. The somewhat unusually form of equation (3.2), with the density $\frac{1}{\rho}$ in front of the term $(\frac{\omega^2}{c^2}-i\beta\omega)\hat{P}$ is intensionally. This form ensures that continuity of particle displacement on fluid interfaces is naturally imposed (Burnett & Zampolli 2003) in the finite element procedure.

Underwater acoustic problems are often posed in an infinite domain, whereas the computational domain must be finite. The computational domain is made finite by the introduction of computational boundaries, which ideally do not influence the solution in the interior domain. There is a balance between the complexity of these boundaries and the computational cost. A "fairly simple" condition can be used if the boundary is located far from the source, at the cost of a large model domain. Limiting the domain, one also has to take into account the complex wave fields near the source (Hodge, Zorumski & Watson 1995). For transient problems, the reflection from such boundaries can be made insignificant within the time period of interest by making the computational domain sufficiently large. For a steady state solution governed by the Helmholtz equation however the time period of interest is in principle infinite.

A transmitted plane wave in the direction n is the solution of the wave equation:

$$\frac{\partial P}{\partial t}+c\frac{\partial P}{\partial n}=0, \tag{3.3}$$

which in the frequency domain reads

$$\frac{\partial\hat{P}}{\partial n}=ik\hat{P}. \tag{3.4}$$

This approach is exact only for waves of normal incidence onto the boundary. The finite element description of this condition will therefore only reduce the reflected field for moderate angles of incidence.

The boundary condition at the bottom can be incorporated in the simulator by the normal specific acoustic impedance, Z_n. Satisfying the boundary conditions at the interface of two fluids amounts to requiring continuity of pressure and continuity of the normal component of particle velocity across the boundary. This is equivalent to requiring continuity of the normal specific acoustic impedance. Because the incident and reflected pressures are not always exactly in or out of phase,

the normal specific acoustic impedance can be complex and frequency dependent (Kinsler, Frey, Coppens & Sanders 2000). It is related to the pressure and velocity by

$$\frac{P}{\vec{v}\cdot\vec{n}} = \frac{P}{|\vec{v}|cos\phi_i} Z_n, \tag{3.5}$$

where $\vec{v}$ is the particle velocity, $\vec{n}$ is the unit vector perpendicular to the interface and ϕ_i is the appropriate angle. The linearized Euler equation (Newton's 2nd law) for the particle velocity is

$$\frac{\partial \vec{v}}{\partial t} = -\frac{1}{\rho_0}\nabla P, \tag{3.6}$$

where ρ_o is the undisturbed density (Jensen, Kuperman, Porter & Schmidt 2000). Removing the time dimension in (3.5) and (3.6) and combining the two equations we obtain the boundary condition for the pressure at the bottom,

$$\frac{\partial \hat{P}}{\partial n} = \frac{i\omega\rho_0}{Z_n}\hat{P}. \tag{3.7}$$

The normal acoustic impedance at the boundary can be expressed in terms of the properties of the incident and reflected waves at the boundary:

$$Z_n = \frac{r_1}{cos\phi_i}\frac{1+R}{1-R}, \tag{3.8}$$

$$R = \frac{r_2 - r_1}{r_2 + r_1}, \tag{3.9}$$

where R is the pressure reflection coefficient and $r_1 = \rho_1 c_1$, $r_2 = \rho_2 c_2$ are the characteristic acoustic impedance of respectively medium 1 (here the water) and medium 2 (the medium on the other side of the interface).

Rigid boundaries, *e.g.* solid sidewalls where $\vec{v}\cdot\vec{n} = 0$, are from the Fourier transform of (3.6) equivalent with:

$$\frac{\partial \hat{P}}{\partial n} = 0. \tag{3.10}$$

This condition corresponds to (3.7) with ($r_1 \ll r_2$)).

Equation (3.5) is also applicable to the surface between water and air. However, since there is a huge difference in material properties between water and air ($r_1 \gg r_2$), the impedance is close to zero. It is therefore assumed that the pressure must vanish at this boundary (the pressure-release condition),

$$\hat{P} = 0. \tag{3.11}$$

3.1 Finite Element Model (*FEM*)

The equation (3.2) with one of the boundary conditions (3.4), (3.7), (3.10) or (3.11) on each boundary define the boundary value problem. However, the radiation condition (3.4) will most

likely pollute the interior solution in simulation with complex topography and a more sophisticated or artificial boundary condition (*ABC*), *e.g.* (Tsynkov 1998), is needed.

A Perfectly Matched Layer (*PML*), proposed by (Berenger 1994), is expected to reduce/eliminate reflections from the open boundaries in the model. An exterior layer at the open boundary is introduced in such a way that all plane waves are absorbed leaving only minor artificial reflection due to the finite extension of the layer, see *e.g.* (Ihlenburg 1998, Turkel & Yefet 1998).

We therefore consider the variable-coefficient Helmholtz equation

$$\nabla \cdot \left(\frac{1}{\rho} \mathbf{A} \nabla \hat{P} \right) + (\frac{\omega^2}{\rho c^2}) \gamma \hat{P} = 0. \tag{3.12}$$

The outline for this equation is given in appendix A. The diagonal matrix $\mathbf{A}$ is given by

$$\mathbf{A}(\mathbf{x}) = diag \left\{ \frac{\gamma(\mathbf{x})}{\gamma_k^2(x_k)} \right\}, \quad \gamma(\mathbf{x}) = \prod_k^3 \gamma_k(x_k), \tag{3.13}$$

where the functions γ_k are of the form

$$\gamma_k(x_k) = 1 + \frac{i\sigma_k(x_k)}{\omega}. \tag{3.14}$$

In the interior domain σ equals to zero and the equation (3.12) reduces to the Helmholtz equation. In the presence of an open boundary the model domain is extended and σ is increased (in our model quadratically) from zero at the location of the original boundary to a finite value at the end of the extended domain, see Figure 3.1.

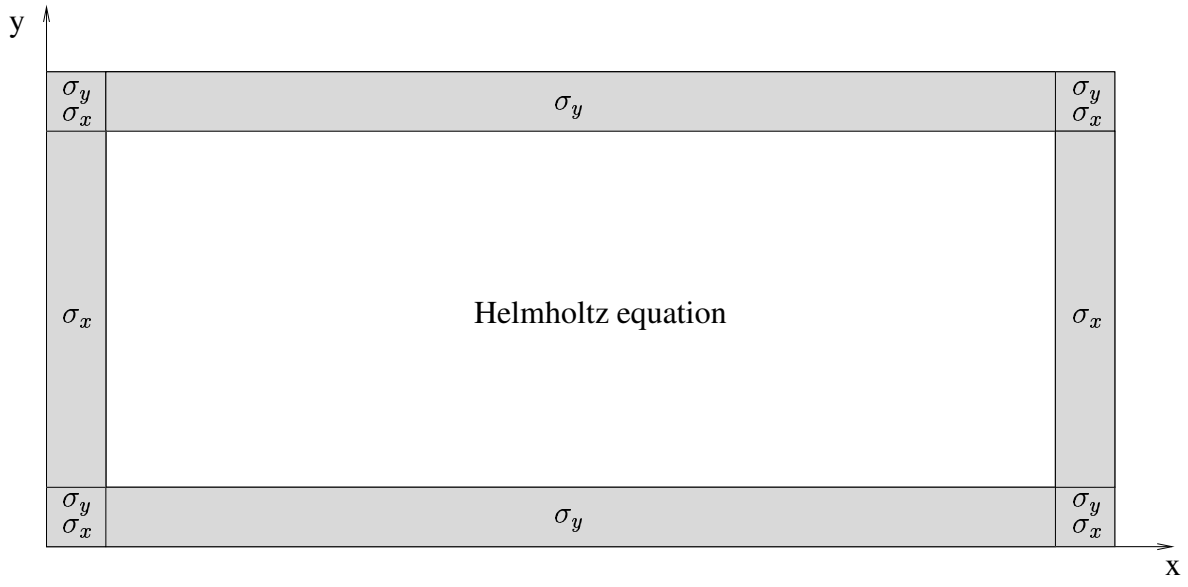

Figure 3.1 Illustration of a computational domain with a Perfectly Matched Layer introduced on all the four open boundaries. Grey areas denote the regions where σ_x and/or σ_y differ from zero.

The variable-coefficient Helmholtz equation (3.12), with the boundary conditions (3.4), (3.7), (3.10) or (3.11), was discretized using Galerkin's method, $\hat{P} \approx \hat{p} = \sum_{j=1}^{M} p_j N_j$, where N_j

denotes the basis functions. The three-dimensional discretization of the variable-coefficient Helmholtz equation results in a large sparse non-Hermitian matrix equation for the pressure in the computational domain on the algebraic form:

$$M_{ij}p_j - K_{ij}p_j + R_{ij}p_j = \int_\Omega f N_i d\Omega, \tag{3.15}$$

$$M_{ij} = \frac{\omega^2}{\rho c^2}\gamma \int_\Omega N_i N_j d\Omega, \tag{3.16}$$

$$K_{ij} = \int_\Omega \mathbf{A}\nabla N_i \cdot \nabla N_j d\Omega, \tag{3.17}$$

$$R_{ij} = \int_{\partial\Omega} \xi N_i N_j d\Gamma. \tag{3.18}$$

Here f accounts for the source term in Helmholtz equation (3.2) and ξ accounts for boundary conditions of type (3.4), (3.7) and (3.10). This linear system with complex coefficient matrix can alternatively be split into its real and imaginary parts and combined into a real system. This has been the prevailing approach when solving complex linear systems and is usually computationally faster than solving the system in its complex form. However, one should read the article by (Freund, Golub & Nachtigal 1992) before implementing (3.15)-(3.18) as a coupled real system. In accordance with the recommendation by (Freund et al. 1992) and (Hodge et al. 1995) we implemented the system in its complex form and used Krylov methods like Generalized Minimal Residual (*GMRES*) or the Transpose-Free Quasi-Minimal Residual (*TFQMR*) methods to solve the equations. For preconditioning, incomplete factorization was primary used to accelerate/enable convergence.

The *FEM* code was implemented with the aid of Diffpack (Langtangen 1999), an object-oriented C++ framework for solving partial differential equations. The resulting simulator has the number of space dimensions parameterized such that the same code applies to 1D, 2D, and 3D problems. To generate mesh in 2D a preprocessor in Diffpack called Preprostdgeom or the program Triangle by Jonathan Richard Shewchuk[1] was used. Preprostdgeom can also generate mesh in simple 3D geometries. For realistic fjord geometries, the GAMBIT CFD Preprocessor by Fluent was used to generate the mesh. For all the simulations presented in this paper a linear tetrahedral mesh is used in the *FEM*. The *FEM* is very flexible in its ability to model wave propagation in very complex and realistic topography. This robustness and flexibility of the model come at a high computational cost.

3.2 Wave Number Integration Model (*WNIM*)

In the wave number integration technique used for the Pekeris wave guide, the integration parameter is the horizontal wave number k_r, where r stands for the radial direction. In the present case, the integration is two dimensional with the integration parameters k_x and k_y, see Figure 3.2. The horizontal wave number is thus given by $k^2_{horizontal} = k^2_{xy} = k^2_x + k^2_y$.

In the following, the symbolism is basically the same as used in the text book by (Jensen et al. 2000). The three dimensional Helmholtz equation, for the velocity potential $\phi = \frac{1}{\rho\omega}P$ is

[1] http://www-2.cs.cmu.edu/∼quake/triangle.html

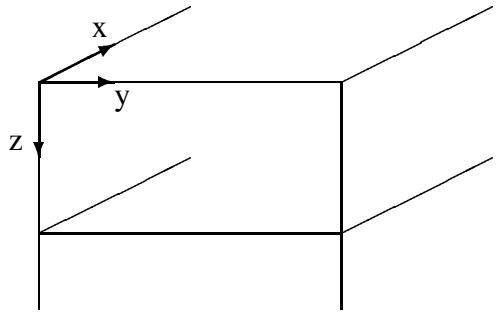

Figure 3.2 Schematic of the geometry

written:

$$(\nabla^2 + k^2)\phi(x, y, z, \omega) = S_\omega \delta(x - x_0)\delta(y - y_0)\delta(z - z_0), \tag{3.19}$$

where x_0, y_0, and z_0 are the coordinates of the source point, and k designates the wave number ω/c.

The x and y dependency of the equation is now transformed to x and y direction wavenumbers by applying a 2 dimensional Fourier transform. As the side walls are supposed hard, and the x coordinate for the source will be taken as zero, the x and y parts of the field will be symmetrical about the origin, and the cosine transform is applied,

$$\Phi(k_x, k_y, z) = \frac{2}{\pi} \int_0^\infty \int_0^\infty \phi(x, y, z) \cos k_x x \cos k_y y \, dxdy. \tag{3.20}$$

This results in the ordinary differential equation:

$$[\frac{d^2}{dz^2} + (k^2 - k_x^2 - k_y^2)]\Phi = \frac{2S_\omega}{\pi} \cos k_x x_0 \cos k_y y_0 \, \delta(z - z_0). \tag{3.21}$$

where k_x and k_y are horizontal wave numbers. The vertical wave number, k_z, is thus expressed via $k_z^2 = k^2 - k_x^2 - k_y^2$.

We assume the water column to have a depth D, and the width of the canal to be L_y. The bottom is of infinite extent.

Introducing k_{xy}^2 as $k_x^2 + k_y^2$, we can write the solution for the upper medium, medium 1, as:

$$\Phi_1(k_{xy}, z) = S_\omega \pi \frac{e^{ik_{z,1}|z-z_0|} \cos k_y y_0}{4ik_{z,1}} + A_1^+(k_{xy}) e^{ik_{z,1}\, z} + A_1^-(k_{xy}) e^{-ik_{z,1}\, z}, \tag{3.22}$$

where the first term represent the particular, and the last two, the homogeneous parts of the solution. The source coordinate x_0 is conveniently set to zero.

In the bottom, the solution must be:

$$\Phi_2(k_{xy}, z) = A_2^+(k_{xy}) e^{ik_{z,2}(z-D)}, \tag{3.23}$$

where the vertical wave number has the form:

$$k_{z,2} = \sqrt{k_2^2 - k_{xy}^2}, \qquad \text{for} \quad |k_{xy}| < k_2,$$
$$k_{z,2} = i\sqrt{k_{xy}^2 - k_2^2}, \qquad \text{for} \quad |k_{xy}| > k_2.$$

Application of the boundary conditions, *i.e.*: vanishing acoustic pressure at the sea surface, and continuity in pressure and normal direction particle velocity at the water/bottom interface give the unknown amplitudes of equations 3.22 and 3.23 via the matrix equation:

$$\begin{bmatrix} 1 & 1 & 0 \\ k_{z,1}e^{ik_{z,1}D} & -k_{z,1}e^{-ik_{z,1}D} & -k_{z,2} \\ \rho_1 e^{ik_{z,1}D} & \rho_1 e^{-ik_{z,1}D} & -\rho_2 \end{bmatrix} \begin{bmatrix} A_1^+ \\ A_1^- \\ A_2^+ \end{bmatrix} = \frac{i\pi S_\omega e^{-ik_y y_0}}{4k_{z,1}} \begin{bmatrix} e^{ik_{z,1}z_0} \\ k_{z,1}e^{ik_{z,1}(D-z_0)} \\ \rho_1 e^{ik_{z,1}(D-z_0)} \end{bmatrix} \tag{3.24}$$

Φ_1 is now transformed back to the x, y, z plane by an inverse cosine transform:

$$\phi_1(x,y,z) = \int_0^\infty \int_0^\infty \Phi_1(k_x, k_y, k_z) \cos k_x x \cos k_y y \; dk_x dk_y. \tag{3.25}$$

Assuming the canal walls, which lay in the $x - z$ planes at $y = 0$ and $y = L_y$, to have homogeneous Neumann boundary conditions (acoustically hard), the only allowed y direction wave numbers are

$$k_y = \frac{n\pi}{L_y}, \quad \text{with} \quad n = 0, 1, 2, 3 \cdots. \tag{3.26}$$

The integral over k_y in the above equation is therefore replaced by a sum over the allowed y direction wave numbers,

$$\phi_1(x,y,z) = \sum_{n=0}^{\infty} \left(\int_0^\infty \Phi_1(k_x, \frac{n\pi}{L_y}, k_z) \cos k_x x \; dk_x \right) \cos \frac{n\pi y}{L_y}. \tag{3.27}$$

To have partially absorbing side walls in the canal, the y direction wave numbers might be modified to incorporate a loss (Morse & Ingard 1986).

4 RESULTS FROM SIMULATIONS

The first and simplest test case is the ideal waveguide described in Jensen et al. (2000, page 110) for a 20 Hz source placed in an open ocean environment with a pressure-release surface and bottom. For this environment the farfield transmission loss should be cylindrical, dropping $3db$ per doubling of distance ($10\log(r)$). Figure 4.1 shows the model result for the *FEM*, sound pressure level (*SPL*). Very good correspondence for this idealized case is found when compared to the analytical *normal-mode expansion* result figure 2.23 of Jensen et al. (2000). Furthermore, a necessary good performance of the artificial open boundaries, the *PML*, is demonstrated. Figure 4.1 also shows the good agreement with pure cylindrical spreading loss, depicted by the solid squares.

In the next simulation the pressure-release bottom is replaced by a penetrable bottom with sound speed $c_2 = 1800$ m/s and density $\rho = 1800$ kg/m^3. This is the so-called Pekeris waveguide

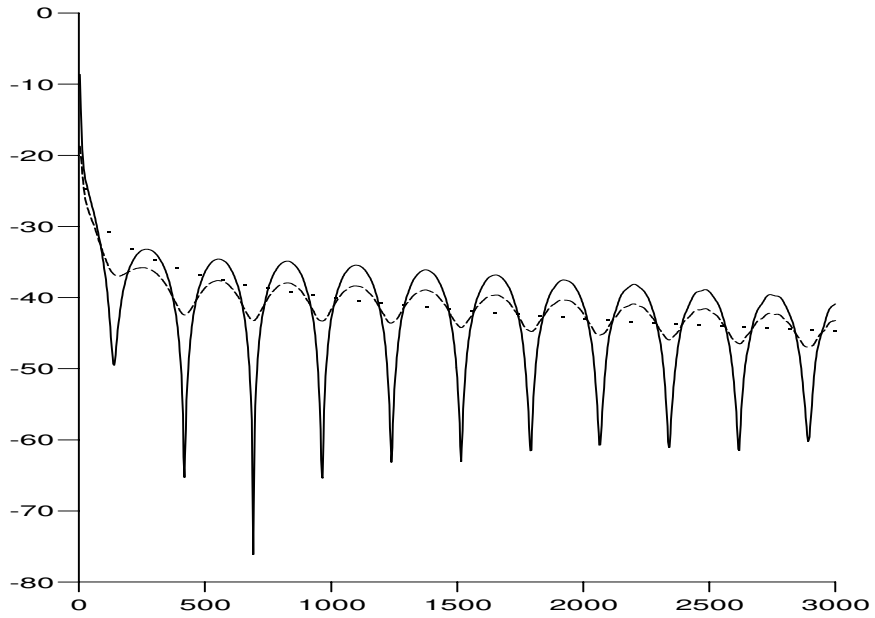

Figure 4.1 Solid curve: Receiver depth 36m. Dashed curve: Receiver depth 46 m. Results from the FEM (SPL vs. range in meter). The solid squares marks a curve corresponding to cylindrical loss. $F = 20$ *Hz.*

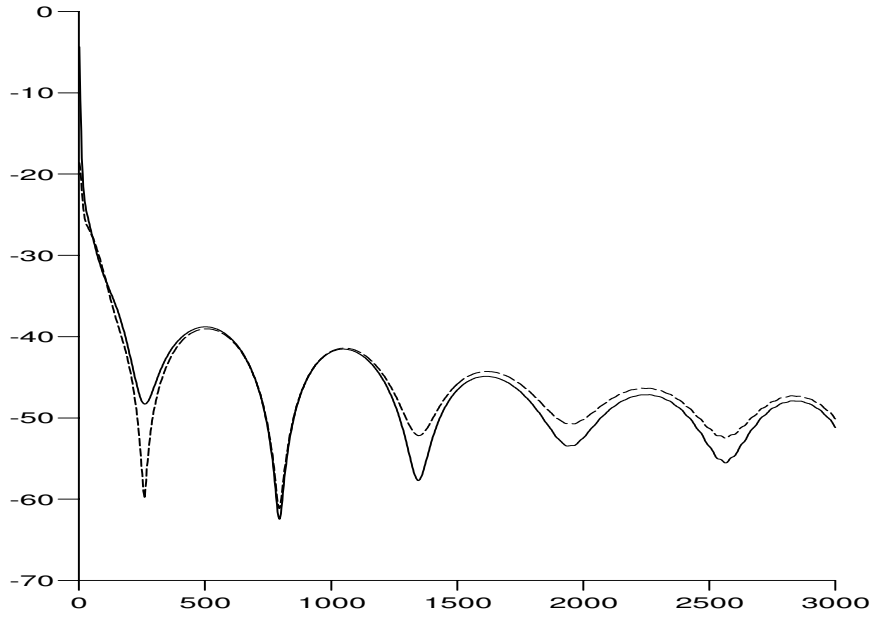

Figure 4.2 Transmission loss. Solid curve: Receiver depth 36m. Dashed curve: Receiver depth 46 m. Results from the FEM (SPL vs. range in meter). $F = 20$ *Hz.*

(Pekeris 1948), and a simulation with a thoroughgoing description of the model setup can be found in Jensen et al. (2000, page 112). The term Pekeris waveguide normally describes a water volume above an infinite fluid half space. Both the water and fluid in the half space are assumed to have constant sound speeds and fluid densities. The water/bottom interface is taken to be plane and horizontal, and the two media are assumed to extend to infinity in the horizontal direction. In several texts, *e.g.* Jensen et al. (2000) and Hovem (2000), the sound propagation in such a geometry is analyzed by a wave number integration technique. Figure 4.2 shows the model result for the *FEM*, which is in very good agreement with the results from the wave number integration model of Jensen et al. (2000, Figure 2.29). It should be mentioned that for the *FEM* the introduction of a sandy bottom increase the computational cost significantly. This is due to the fact that one also has to calculate the propagation in a sufficiently large bottom layer to get the correct interaction on the interface between the two media. For this particular simulation we introduced a bottom layer column with a depth of 130 meters connected to a *PML* in the bottom.

For the next idealized test case, the geometry also includes parallel side walls, thereby changing the geometry to that of a canal. A sketch of our Pekeris Canal for benchmarking the *FEM* and the *WNIM* is depicted in Figure 3.2. Further description of the simulation environment is found in Table 4.1.

Table 4.1 Description of the model environment for the Pekeris canal.

Parameter	Notation	Value
Water column depth	D	100 m
Width	L_y	100 m
Source Depth	S	(0,50,36)
Frequency	F	20 Hz
Density Water	ρ_1	1000 kg/m^3
Density bottom layer	ρ_2	1800 kg/m^3
Speed of sound water	c_1	1500 m/s
Speed of sound bottom layer	c_2	1800 m/s
Receiver Depth 1 (line)	RD1	(2,50,36) $\rightarrow$ (1000,50,36)
Receiver Depth 2 (line)	RD2	(2,50,46) $\rightarrow$ (1000,50,46)
Receiver Depth 3 (line)	RD3	(2,75,36) $\rightarrow$ (1000,75,36)

Figures 4.3 and 4.4 show the sound pressure level in the Pekeris canal described in Table 4.1. For the *FEM* the sand layer has a thickness of 100 meter ending in a *PML* with thickness 24 meters.

The left figure in 4.5 shows the sound pressure level as function of range for a frequency of 1 Hz. The upper curve of the right hand side of 4.5 show the pressure levels for 80 Hz. In the lower curve we have artificially included an extreme damping in the sand (Loss tangent=0.2, (Jensen et al. 2000)), to study the effect on the results.

In certain situations the sea bottom might be so complex (containing large individual rocks, the geological strata might be almost vertical giving a rugged sand covered bottom *etc.*) so that waves cannot be expected to propagate freely in the horizontal direction in the sea bottom. An attempt to

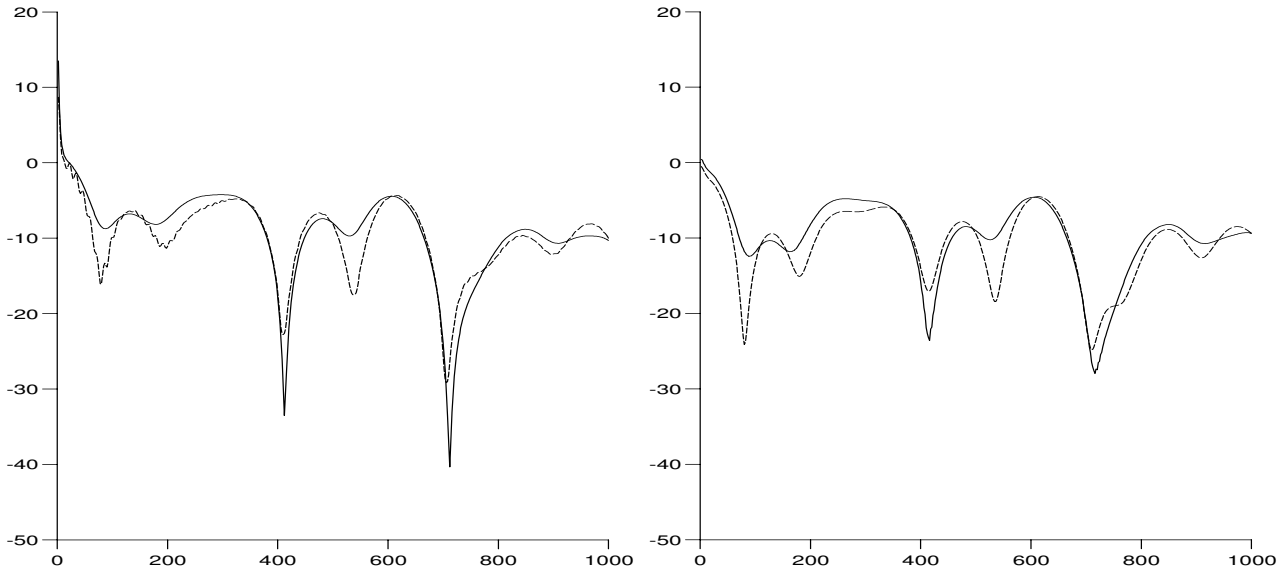

Figure 4.3 SPL vs. range in meter, left panel RD1, right panel RD2. Dashed line WNIM, solid FEM. $F = 20$ *Hz.*

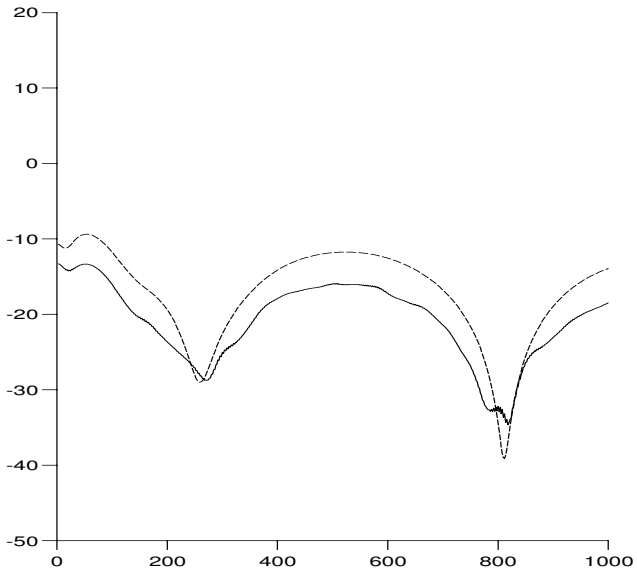

Figure 4.4 SPL vs. range in meter, RD3. Dashed line WNIM, solid FEM. $F = 20$ *Hz.*

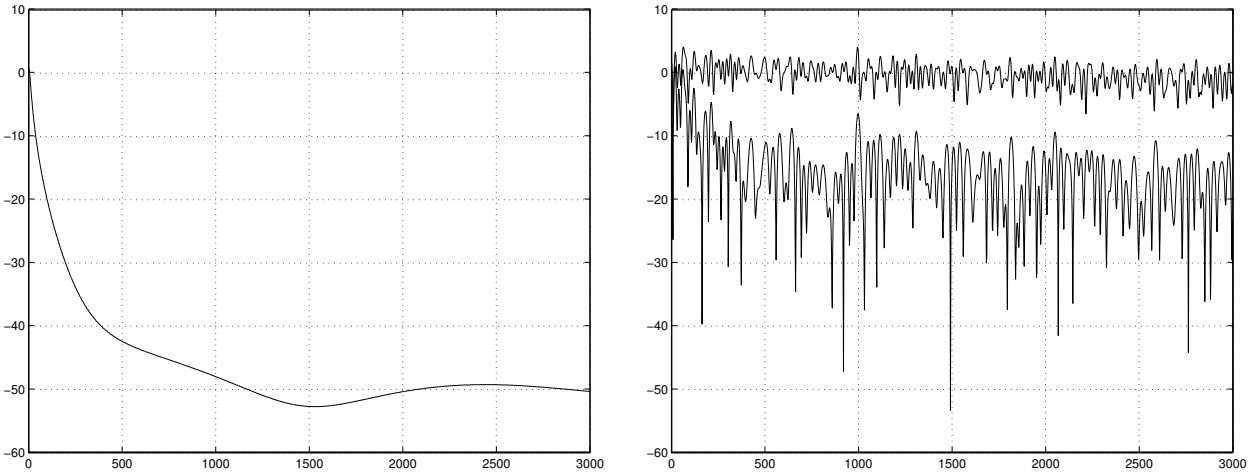

Figure 4.5 SPL vs. range in meter; Left panel RD2 for a source with frequency 1 HZ. Right panel RD2 for a source with frequency 80 HZ. Upper line loss tangent in sand equal to 0.002. Lower line loss tangent in sand equal to 0.2. All lines from simulations by WNIM.

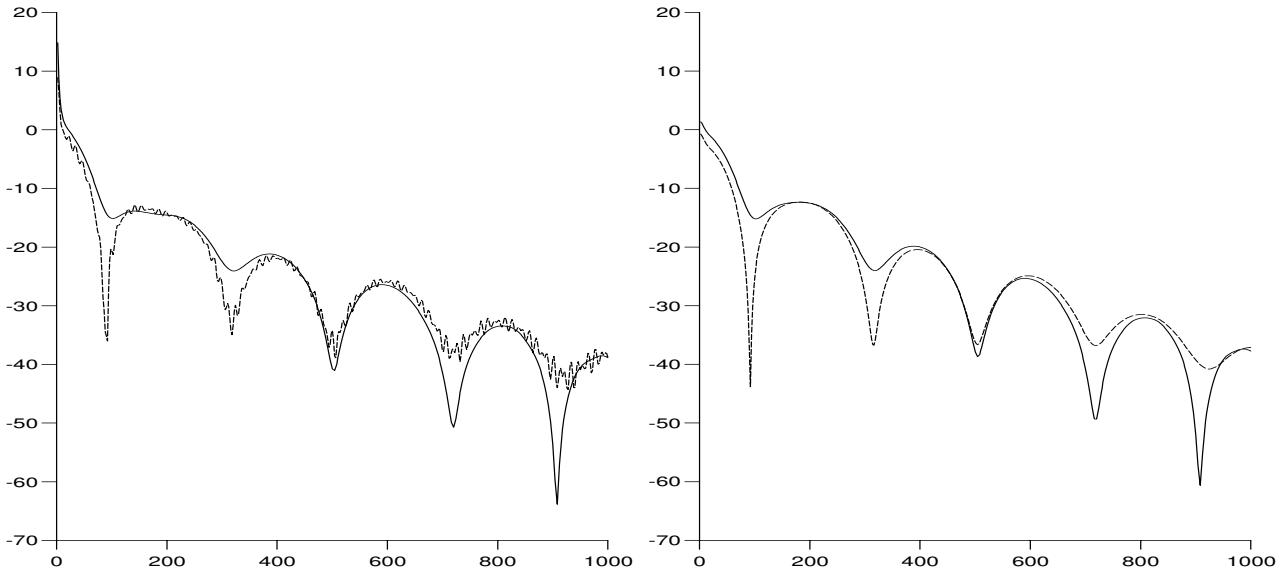

Figure 4.6 SPL vs. range in meter, left panel RD1, right panel RD2. Dashed line WNIM, solid FEM. Constant normal direction impedance at the seafloor. $F = 20$ Hz.

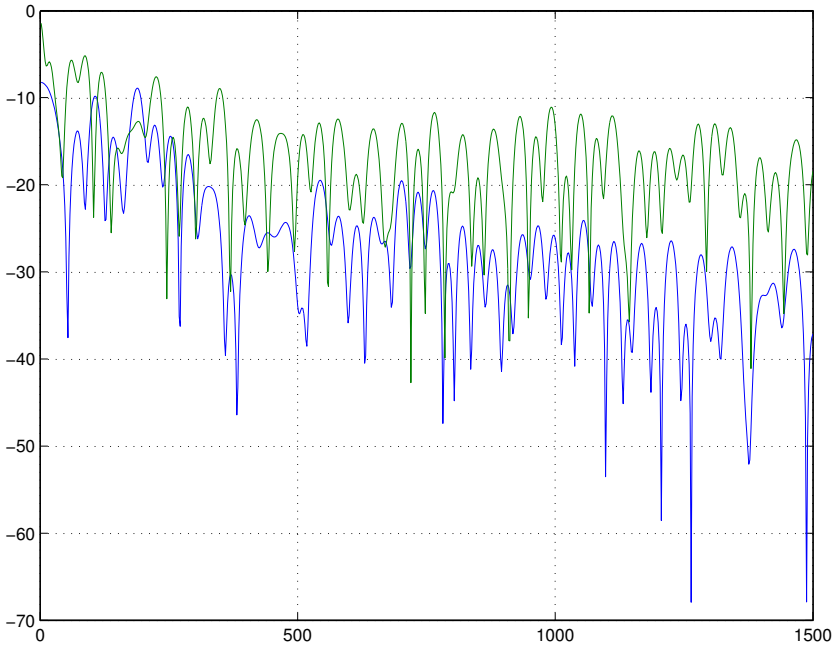

Figure 4.7 *SPL vs. range in meter, Green curve RD2, Blue curve receiver depth at 99.5 m. $F = 80$ Hz.*

study such situations might be to give the bottom a constant normal direction impedance ($Z_n = \rho_2 c_2$, $\phi_i = 0$ equation 3.5). Such a condition is often termed a locally reacting interface (Salomons 2001) *i.e.* the wave impedance met at the bottom is not influenced by waves propagating horizontally in the lower medium. Other terms used in the literature are "normally reacting surface" (Mackenzie 1960) and "constant normal impedance boundary" (Lawhead & Rudnick 1951). Model results with such a constant normal direction impedance are shown in Figure 4.6 for the *FEM* and *WNIM*.

It is seen that waves propagating in a canal having this type of bottom, generally has a higher loss than for the horizontally stratified canals. At low frequencies this is seen for both the receiver depths, while for the frequency 80 Hz, it is especially along the bottom this is observed, Figure 4.7. It should also be mentioned that changing the normal impedance values to the values of limestone had only a minor influence on the result.

4.1 Further calculations using the *FEM* model

Conventional propagation models, discussed by *e.g.* (Jensen 1984), are not applicable in realistic coastal environments, typically characterized as a long and narrow, possibly deep, confined fjord with a very spatially dependent topography.

In the autumn of 2002, the Norwegian Defence Research Establishment conducted a measurement campaign in Fesøysundet. The acoustic field from controllable sources (Baker source, imploding light-bulbs, etc.), the depth topography and geoacoustic properties were measured. Figure 4.8 and 4.9 show modeled *SPL* from the *FEM*, respectively for a horizontal and a vertical cross section of Fesøysundet. The model domain, spanning approximately 1460 m x 480 m in the horizontal with a maximum depth of 84 meter, is resolved by 1823409 tetrahedrals.

For simplicity, total reflection from the bottom and sidewalls are assumed. A *PML* is introduced at the open boundaries with a length of 50 meters. For such complex topographies the finite element approach is very well suited. In the near future, a study comparing *FEM* simulations (with more realistic bottom condition) from Fesøysundet and measurements will be conducted.

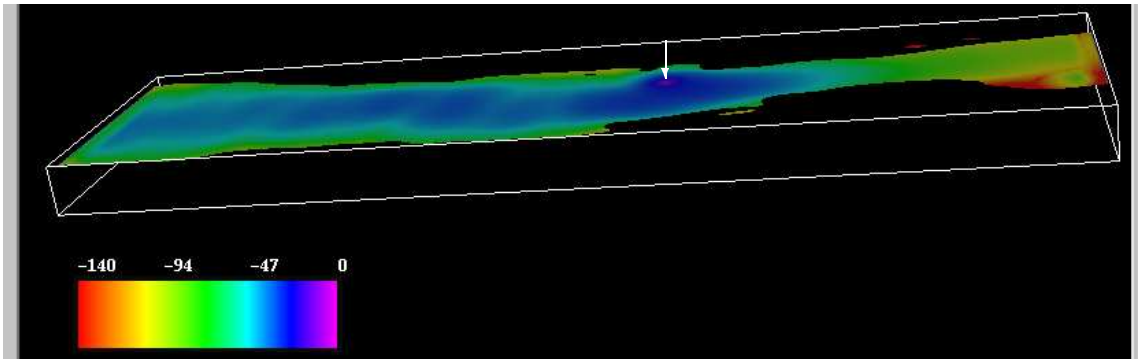

Figure 4.8 *SPL. The point source with frequency 10 HZ is located 20 meter below the surface. This horizontal cross section is taken in the plane of the source. The source coordinates are (600,230,-20) and is located on the figure by the white arrow.*

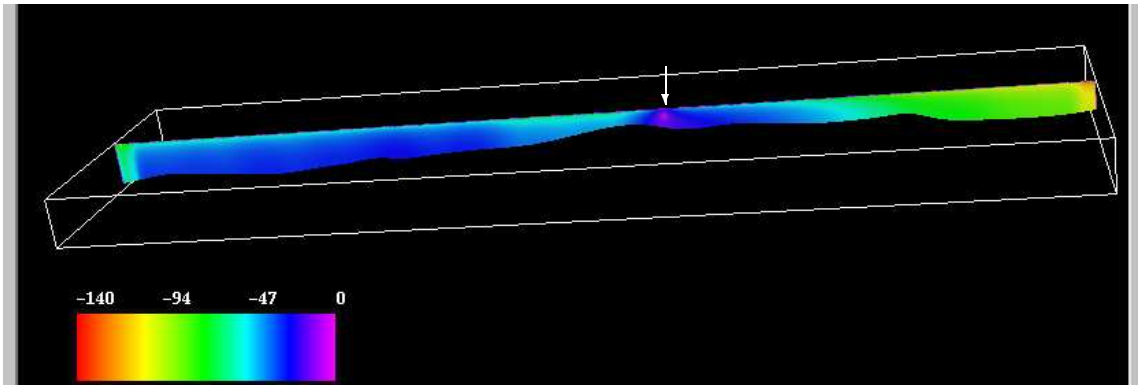

Figure 4.9 *SPL. The point source with frequency 10 HZ is located 20 meter below the surface. This vertical cross section is taken in the plane of the source. The source coordinates are (600,230,-20) and is located on the figure by the white arrow.*

5 DISCUSSION AND CONCLUSIONS

From the results section, we see that the two models give close results. Levels are adjusted by eye so that the curves for the two models are as close as possible. The reason for this is that the source strengths are not the same in the two models. From figures 4.3 and 4.4, we see that the peaks and troughs appear at the same ranges. Peaks correspond to constructive interference between the different modes of the canal, while troughs correspond to destructive interference. We see also that particularly the destructive interference levels differ between the models. This might be caused by the slight difference in source descriptions. The finite element model has its source distributed over the nearest neighboring elements, while the source in the wave number integration model is a true point source. Experiments with grid-refinements near the source for the *FEM* showed that even better agreement between the models can be obtained.

It is useful to discuss the results from the point of view of modes. These modes are made up by wave interference effects in the depth and across canal directions. The pure depth modes have the

pressure release water - air interface and the continuity conditions at the sea bottom as boundary conditions, while the across canal modes are pure cosine distributions due to the acoustically hard walls assumed in the model.

The geometry used in the figures is a 100m deep and 100m wide canal extending to infinity in both directions, see table 4.1. The left figure in 4.5 shows the sound pressure level as function of range (horizontal distance) for a frequency of 1 Hz. It is seen that the level decreases with about 6 dB per doubling of distance up to a distance of about 1000 m. At further distances, the level is nearly constant. In the model there is a slight damping included in the bottom sand (it is assumed a loss tangent of 0.002). At this frequency, there is no interaction between modes in the canal.

The 20 Hz results show distinct interaction patterns. The 0'th, 1st, and 2nd modes are possible in the across canal direction, corresponding to constant, and the cosine distributions given by one half, and one complete wavelength. For the calculated example, with the source in the mid plane, the 1st mode will not be excited. Three depth direction modes are also possible. The 20 Hz figure at $y = 25$ m shows the pressure distribution to be simpler than at $y = 50$ m, this is due to the fact that the 2nd across canal mode has a node at this position. It should also be mentioned that the small oscillations seen at on the curves calculated by the wave number integration technique for the depth 36 m is caused by slow convergence in the integration procedure for receivers and sources having the same depth.

The upper curve on the right hand side of Figure 4.5 show the pressure levels for 80 Hz, calculated by the wave number integration technique. For this frequency many modes are active and the distinct interference effects are averaged out. The level appears constant as the model does not include much damping. In the lower curve we have artificially included an extreme damping in the sand (Loss tangent=0.2), to study the effect on the results. We see a -6 dB per doubling of distance behavior up to a certain range and thereafter a fairly constant level. In this far from source region the wave field is possibly made up by primarily across canal wave motion. In real life the side walls will not appear as completely hard walls, they will provide both damping and diffusion, and we would expect results similar to Figure 4.5 for a horizontally layered sand bottom in this frequency range.

Figures 4.6, and 4.7 show results for a sea bottom having a so called constant normal impedance, in this case the specific impedance of sand. Such a bottom will be much more absorptive than in the normal Pekeris case. It is included because an earlier measuring campaign indicated that this type of conditions might be present in Norwegian fjords and straits. Physically it corresponds to the assumption that waves in the bottom are propagated at normal direction to the sea bed, *i.e.* vertically down. The decrease in level is close to 12db per doubling of distance $-40logR$. At 20 Hz this effect is seen for both the calculated depths (36 m and 46 m), while for the 80 Hz example the effect is particularly noticeable close to the sea bottom (99.5 m).

Figures 4.8 and 4.9 are demonstrations of the capability of the finite element technique to model realistic geometries. In general, solving the large nonsymetric linear system derived from the finite element formulation of the Helmholtz equation can be difficult. Some iterative attempts in finding a suitable preconditioner and solver must therefore be taken into account when using this *FEM*.

References

(1) Berenger J P (1994): A Perfectly Matched Layer for the Absorption of Electromagnetic Waves, *Journal of Computational Physics* **114**, 185–200.

(2) Brodtkorb P A, Jenssen A J (2002): MacBeth - a Marine Acoustic Beam Tracer, 'Proceedings of Scandinavian Symposium of Physical Acoustics, Ustaoset, Norway'.

(3) Burnett D S, Zampolli M (2003): Development of a finite-element, steady-state 3-D acoustics code for target scattering, Technical Report SR-379, Saclant Undersea Research Centre.

(4) Freund R W, Golub G H, Nachtigal N M (1992): Iterative Solution of Linear Systems, *Acta Numerica* **1**, 57–100.

(5) Hodge S L, Zorumski W E, Watson W R (1995): Solution of the Three-Dimensional Helmholtz Equation With Nonlocal Boundary Conditions, TECHNICAL REPORT, NASA.

(6) Hovem J M (2000): 'Marin akustikk', Kompendium Institutt for Teleteknikk, (In Norwegian).

(7) Ihlenburg F (1998): Finite Element Analysis of Acoustic Scattering, Vol. 132 of *Applied Mathematical Sciences*, Springer.

(8) Jensen F B (1984): Numerical models in underwater acoustics, L. B.Felsen, ed., 'Hybrid Formulation of Wave Propagation and Scattering', 1 edn, number 86 *in* 'NATO ASI Series, Series E: Applied Science', Martinus Nijhoff Publishers.

(9) Jensen F B, Kuperman W A, Porter M B, Schmidt H (2000): Computational ocean acoustics, Springer-Verlag.

(10) Kinsler L E, Frey A R, Coppens A B, Sanders J V (2000): Fundamentals of Acoustics, John Wiley & Sons.

(11) Langtangen H P (1999): Computational Partial Differential Equations, Springer.

(12) Lawhead R B, Rudnick I (1951): Acoustic Wave Propagation Along a Constant Normal Impedance Boundary, *The Journal of the Acoustic Society of America* **23**(5).

(13) Mackenzie K (1960): Reflection of Sound from Coastal Bottoms, *Journal of the Acoustical Society of America* **32**, 221–231.

(14) Morse P M, Ingard K U (1986): Theoretical Acoustics, Princeton University Press, Princeton, New Jersey, USA.

(15) Ommundsen A (2003): Numerical solution of the Helmholtz equation for underwater acoustics in fjords and straits, B.Skallerud, H. I.Andersson, eds, 'MekIT'03', Second national conference on Comutational Mechanics, Tapir Academic Press, pp. 275–283.

(16) Pekeris C L (1948): Theory of propagation of explosive sound in shallow water, *The Geological Society of America Memoir* **27**.

(17) Salomons E M (2001): Computational Atmospheric Acoustics, Springer.

(18) Tsynkov S V (1998): Numerical solution of problem on unbounded domains, *Applied Numerical Mathematics* **27**, 465–532.

(19) Turkel E, Yefet A (1998): Absorbing PML boundary layers for wave-like equations, *Applied Numerical Mathematics* **27**, 533–557.

APPENDIX

A PERFECTLY MATCHED LAYER (*PML*) THE EQUATIONS

The linearized continuity equation reads,

$$\frac{\partial \rho}{\partial t} + \rho_0 \nabla \cdot \mathbf{V} = \mathbf{0}. \tag{A.1}$$

Introducing $\rho = \rho_x + \rho_y + \rho_z$, where ρ_x, ρ_y and ρ_z are just formal variables with no physical meaning we rewrite (A.1) as a system

$$\frac{\partial \rho_x}{\partial t} = -\rho_0 V_{x,x} \quad , \quad \frac{\partial \rho_y}{\partial t} = -\rho_0 V_{y,y} \quad , \quad \frac{\partial \rho_z}{\partial t} = -\rho_0 V_{z,z} \tag{A.2}$$

The linearized Euler equations (3.6) for each component are

$$\frac{\partial V_x}{\partial t} = -\frac{1}{\rho_0}\frac{\partial P}{\partial x} \quad , \quad \frac{\partial V_y}{\partial t} = -\frac{1}{\rho_0}\frac{\partial P}{\partial y} \quad , \quad \frac{\partial V_z}{\partial t} = -\frac{1}{\rho_0}\frac{\partial P}{\partial z} \tag{A.3}$$

and the pressure and density are coupled by the material law

$$P = c^2 \rho. \tag{A.4}$$

Absorption terms $\sigma_x(x), \sigma_y(y)$ and $\sigma_z(z)$ are added to the system (A.2)

$$\frac{\partial \rho_x}{\partial t} + \sigma_x(x)\rho_x = -\rho_0 V_{x,x} \quad , \quad \frac{\partial \rho_y}{\partial t} + \sigma_y(y)\rho_y = -\rho_0 V_{y,y} \quad , \quad \frac{\partial \rho_z}{\partial t} + \sigma_z(z)\rho_y = -\rho_0 V_{z,z} \tag{A.5}$$

Based on this approach and by replacing the time-derivatives with $-i\omega$ the *PML* equation for the time-harmonic equation can be formulated as:

$$\begin{aligned} &\frac{\partial}{\partial x}\left(\frac{(\sigma_y - i\omega)(\sigma_y - i\omega)}{\sigma_x - i\omega}\frac{\partial P}{\partial x}\right) + \frac{\partial}{\partial y}\left(\frac{(\sigma_x - i\omega)(\sigma_z - i\omega)}{\sigma_y - i\omega}\frac{\partial P}{\partial y}\right) + \\ &\frac{\partial}{\partial z}\left(\frac{(\sigma_x - i\omega)(\sigma_y - i\omega)}{\sigma_z - i\omega}\frac{\partial P}{\partial z}\right) - c^{-2}(\sigma_x - i\omega)(\sigma_y - i\omega)(\sigma_y - i\omega)P = 0 \end{aligned}$$